# Light concentration in the near-field of dielectric spheroidal particles with mesoscopic sizes

**Manuel J. Mendes,\* Ignacio Tobías, Antonio Martí, and Antonio Luque**

*Instituto de Energía Solar, E.T.S.I. Telecomunicación, Universidad Politécnica de Madrid, Ciudad Universitaria, Avda. Complutense 30, 28040 Madrid, Spain*
*\*manuel.mendes@ies-def.upm.es*

**Abstract:** This paper presents a numerical study of the light focusing properties of dielectric spheroids with sizes comparable to the illuminating wavelength. An analytical separation-of-variables method is used to determine the electric field distribution inside and in the near-field outside the particles. An optimization algorithm was implemented in the method to determine the particles' physical parameters that maximize the forward scattered light in the near-field region. It is found that such scatterers can exhibit pronounced electric intensity enhancement (above 100 times the incident intensity) in their close vicinity, or along wide focal regions extending to 10 times the wavelength. The results reveal the potential of wavelength-sized spheroids to manipulate light beyond the limitations of macroscopic geometrical optics. This can be of interest for several applications, such as light management in photovoltaics.

©2011 Optical Society of America

**OCIS codes:** (290.5850) Scattering, particles; (260.2110) Electromagnetic optics; (040.5350) Photovoltaic.

## References and links

1. C. Girard and A. Dereux, "Near-field optics theories," Rep. Prog. Phys. **59**(5), 657–699 (1996).
2. L. Novotny and B. Hecht, *Principles of Nano-Optics* (Cambridge University Press, 2006).
3. M. J. Mendes, I. Tobías, A. Martí, and A. Luque, "Near-field scattering by dielectric spheroidal particles with sizes on the order of the illuminating wavelength," J. Opt. Soc. Am. B **27**(6), 1221–1231 (2010).
4. C. F. Bohren and D. R. Huffman, *Absorption and Scattering of Light by Small Particles* (Wiley-VCH, 2004).
5. H. Mertens, A. F. Koenderink, and A. Polman, "Plasmon-enhanced luminescence near noble-metal nanospheres: comparison of exact theory and an improved Gersten and Nitzan model," Phys. Rev. B **76**(11), 115123 (2007).
6. Z. Chen, A. Taflove, and V. Backman, "Photonic nanojet enhancement of backscattering of light by nanoparticles: a potential novel visible-light ultramicroscopy technique," Opt. Express **12**(7), 1214–1220 (2004).
7. C. Li, G. W. Kattawar, P.-W. Zhai, and P. Yang, "Electric and magnetic energy density distributions inside and outside dielectric particles illuminated by a plane electromagnetic wave," Opt. Express **13**(12), 4554–4559 (2005).
8. J. Grandidier, D. M. Callahan, J. N. Munday, and H. A. Atwater, "Thin-film solar cells: light absorption enhancement in thin-film solar cells using whispering gallery modes in dielectric nanospheres," Adv. Mater. (Deerfield Beach Fla.) **23**(10), 1171 (2011).
9. L. E. McNeil, A. R. Hanuska, and R. H. French, "Near-field scattering from red pigment particles: absorption and spectral dependence," J. Appl. Phys. **89**(3), 1898–1906 (2001).
10. S. Lecler, Y. Takakura, and P. Meyrueis, "Properties of a three-dimensional photonic jet," Opt. Lett. **30**(19), 2641–2643 (2005).
11. J. Kofler and N. Arnold, "Axially symmetric focusing as a cuspoid diffraction catastrophe: scalar and vector cases and comparison with the theory of Mie," Phys. Rev. B **73**(23), 235401 (2006).
12. H. J. Münzer, M. Mosbacher, M. Bertsch, J. Zimmermann, P. Leiderer, and J. Boneberg, "Local field enhancement effects for nanostructuring of surfaces," J. Microsc. **202**(1), 129–135 (2001).
13. A. Devilez, N. Bonod, and B. Stout, "Near field dielectric microlenses," Proc. SPIE **7717**, 771708 (2010).
14. M. Born and E. Wolf, *Principles of Optics: Electromagnetic Theory of Propagation, Interference and Diffraction of Light,* 7th ed. (Cambridge University Press, 1999).
15. L.-W. Li, X.-K. Kang, and M.-S. Leong, *Spheroidal Wave Functions in Electromagnetic Theory* (John Wiley & Sons, Inc., 2002).
16. J. P. Barton, "Internal and near-surface electromagnetic fields for a spheroidal particle with arbitrary illumination," Appl. Opt. **34**(24), 5542–5551 (1995).
17. A. Devilez, N. Bonod, J. Wenger, D. Gérard, B. Stout, H. Rigneault, and E. Popov, "Three-dimensional subwavelength confinement of light with dielectric microspheres," Opt. Express **17**(4), 2089–2094 (2009).
18. A. V. Itagi and W. A. Challener, "Optics of photonic nanojets," J. Opt. Soc. Am. A **22**(12), 2847–2858 (2005).

19. A. Devilez, B. Stout, N. Bonod, and E. Popov, "Spectral analysis of three-dimensional photonic jets," Opt. Express **16**(18), 14200–14212 (2008).
20. P. Ferrand, J. Wenger, A. Devilez, M. Pianta, B. Stout, N. Bonod, E. Popov, and H. Rigneault, "Direct imaging of photonic nanojets," Opt. Express **16**(10), 6930–6940 (2008).
21. S. Lecler, "Light scattering by sub-micrometric particles," PhD thesis (Louis Pasteur University, 2005).
22. E. Hecht, *Optics,* 4th ed. (Addison Wesley, 2001).
23. S. Asano and G. Yamamoto, "Light scattering by a spheroidal particle," Appl. Opt. **14**(1), 29–49 (1975).
24. E. M. Purcell and C. R. Pennypacker, "Scattering and absorption of light by nonspherical dielectric grains," Astrophys. J. **186**(2), 705–714 (1973).
25. J. C. Ravey and P. Mazeron, "Light-scattering in the physical optics approximation—application to large spheroids," J. Opt. **13**(5), 273–282 (1982).
26. J. P. Barton, "Internal, near-surface, and scattered electromagnetic fields for a layered spheroid with arbitrary illumination," Appl. Opt. **40**(21), 3598–3607 (2001).
27. N. Richard, "Analysis of polarization effects on nanoscopic objects in the near-field optics," Phys. Rev. E Stat. Nonlin. Soft Matter Phys. **63**(2), 026602 (2001).
28. J. P. Barton, "Internal and near-surface electromagnetic fields for an absorbing spheroidal particle with arbitrary illumination," Appl. Opt. **34**(36), 8472–8473 (1995).
29. T. D. Milster, "Near-field optical data storage: avenues for improved performance," Opt. Eng. **40**(10), 2255–2260 (2001).
30. A. Devilez, B. Stout, and N. Bonod, "Compact metallo-dielectric optical antenna for ultra directional and enhanced radiative emission," ACS Nano **4**(6), 3390–3396 (2010).
31. M. J. Mendes, A. Luque, I. Tobias, and A. Marti, "Plasmonic light enhancement in the near-field of metallic nanospheroids for application in intermediate band solar cells," Appl. Phys. Lett. **95**(7), 071105 (2009).
32. C. Flammer, *Spheroidal Wave Functions* (Stanford University Press, 1957).
33. L. W. Li, M. S. Leong, T. S. Yeo, P. S. Kooi, and K. Y. Tan, "Computations of spheroidal harmonics with complex arguments: a review with an algorithm," Phys. Rev. E Stat. Phys. Plasmas Fluids Relat. Interdiscip. Topics **58**(5), 6792–6806 (1998).
34. P. Kirby, "Calculation of spheroidal wave functions," Comput. Phys. Commun. **175**(7), 465–472 (2006).
35. R. Kirby, "Calculation of radial prolate spheroidal wave functions of the second kind," Comput. Phys. Commun. **181**(3), 514–519 (2010).
36. H. A. Atwater and A. Polman, "Plasmonics for improved photovoltaic devices," Nat. Mater. **9**(3), 205–213 (2010).
37. C. Hägglund and B. Kasemo, "Nanoparticle plasmonics for 2D-photovoltaics: mechanisms, optimization, and limits," Opt. Express **17**(14), 11944–11957 (2009).
38. A. Luque, A. Marti, M. J. Mendes, and I. Tobias, "Light absorption in the near field around surface plasmon polaritons," J. Appl. Phys. **104**(11), 113118 (2008).
39. J. Y. Lee and P. Peumans, "The origin of enhanced optical absorption in solar cells with metal nanoparticles embedded in the active layer," Opt. Express **18**(10), 10078–10087 (2010).
40. C. Cohen-Tannoudji, J. Dupont-Roc, and G. Grynberg, *Photons and Atoms—Introduction to Quantum Electrodynamics* (Wiley-Interscience, 1997).
41. P. Mazeron and S. Muller, "Dielectric or absorbing particles: EM surface fields and scattering," J. Opt. **29**(2), 68–77 (1998).
42. J. C. Lagarias, J. A. Reeds, M. H. Wright, and P. E. Wright, "Convergence properties of the Nelder-Mead simplex method in low dimensions," SIAM J. Optim. **9**(1), 112–147 (1998).
43. M. J. Mendes, H. K. Schmidt, and M. Pasquali, "Brownian dynamics simulations of single-wall carbon nanotube separation by type using dielectrophoresis," J. Phys. Chem. B **112**(25), 7467–7477 (2008).

## 1. Introduction

Near-field effects become particularly important when the size of the scattering object is smaller or on the order of the illuminating wavelength ($\lambda$), therefore outside the macroscopic regime of geometrical optics (GO) [1–3]. The field distribution produced by objects with sizes much smaller than $\lambda$ can be obtained with the electrostatic approximation (EA) [4]. Scatterers in this size regime produce dipolar-like (first order) near-field patterns independently of their geometry or material. As the particle size approaches $\lambda$, higher order modes (quadrupolar, octopolar, etc.) are excited producing additional features in the field pattern which are highly dependent on the scatterer physical parameters (size, shape, material and surrounding medium) [4,5]. In this paper we focus on particles with sizes on the order of $\lambda$, which lie in an intermediate scattering regime between EA and GO – the mesoscopic regime. This regime is still rather unexplored, since the solution of electromagnetic (EM) scattering by mesoscopic objects requires the detailed calculation of the full set of Maxwell's equations [1,3].

Numerical grid-based approaches, such as finite difference time-domain (FDTD) [6–8] and finite elements methods (FEM) [9], are often employed to model the near-field distribution of complex mesoscopic structures. However, with mesh approaches it is usually

difficult to resolve high field gradients that occur at the surface of particles that scatter highly resonantly with the incident light. Therefore, whenever possible, it is preferable to use analytical techniques since the fields can be calculated everywhere without needing to cope with finite mesh resolution errors. Most of the analytical studies published so far on light scattering by mesoscopic particles use Mie theory [4,10–14], which is valid for any particle size but restricted to perfectly spherical shapes. In the present work, a spheroidal coordinate separation-of-variables solution is used to study the near-field scattering properties of spheroidal particles with arbitrary size and shape [3,15,16].

Objects with sizes close to or above λ scatter the light preferentially along the incident wave propagation direction (forward scattering). Dielectric spheres and cylinders have been shown [6,7,9,10,12,17–19] to produce remarkably intense electric fields close to their shadow-side surface. They act as near-field lenses concentrating the light in a jet-like region located along the incidence axis, which has already been corroborated experimentally by direct imaging [20]. The laws of such focusing are quite distinct from those of macroscopic GO lenses [11,12,18,21]. In the mesoscopic regime the diffraction pattern is dictated by EM wave interference mechanisms which redistribute the energy from the regions of destructive interference to those of constructive interference [22], as discussed in Section 3.

In most cases of practical interest scatterers are non-spherical and can be better approximated by a spheroidal shape. However, accurate light-scattering computations for mesoscopic spheroids are complex and time consuming, and the literature in which such calculations are reported is rather scarce. The work presented in this paper contributes to fulfil this gap. The near-field light focusing properties of dielectric spheroids with arbitrary size, aspect ratio and complex refractive index are analysed; and important additional possibilities are found relative to the particular case of spheres. A small imaginary part is considered in the materials refractive index in order for the results to meet conditions attainable in practice.

The possibility to concentrate light in the near-field of dielectric mesoscopic particles (DMPs) is still little explored [11,21]. This is partly due to the fact that usually only their far-field scattering properties are studied [15,23–25]. Besides, the high energy concentration occurs only in specific cases when there is an optimized set of physical parameters that allow a pronounced constructive interference in the diffraction pattern. In any application, the absorptive nature of scatterers and the high confinement of their near-field substantially limit the parameter space where near-field structures can provide exceptional improvements to the properties of the surrounding receiving materials (emitters or absorbers depending on the application) [5]. Therefore, a theoretical study involving a computational optimization is crucial prior to any practical implementation. In this paper, an optimization algorithm was developed that iteratively searches for the DMP parameters that provide the highest possible forward scattered field intensities along a certain region of the external medium.

Previous works on scattering by mesoscopic spheroids already investigated some properties of their near-field distributions [3,7,16,26]. However, this article is the first contribution, to our knowledge, presenting an optimization study which seeks the best electric energy focusing characteristics that can be produced by such particles. The evolution of the optimization process towards convergence provides important insight about the role that each DMP parameter (size, aspect ratio and material contrast) plays on the characteristics of the near-field distribution. For particular parameter sets the field outside the particle can achieve intensities more than two orders of magnitude higher than the incident intensity. Furthermore, the spatial location and extension of such field enhancement can be controlled [3], allowing distinct types of field patterns ranging from highly confined and intense focal spots to less intense but widely spread focal regions.

This can be of interest for several applications such as nanoscale processing of materials (ablation [12] or photo-etching [11]), high-resolution microscopy (e.g. biomedical diagnostics [6,27]), resonance spectroscopy (e.g. amplification of Raman and fluorescence [7,28] signals), localized sensing techniques (e.g. enhancement of nanoparticles backscattering [9,13]), optical data storage [29], optical antennas [30], among others. Nevertheless, the authors are particularly interested in its implementation in photovoltaic devices [31]. The incorporation of

DMPs as "mesoscopic lenses" in a solar cell could lead to locally enhanced optical absorption and an overall increase in the power conversion efficiency [8]. The increased strength of the optical interactions with the PV material would also allow the use of a thinner (thus less expensive) photo-active region.

## 2. Separation-of-variables method and definitions

We consider the EM interaction between a spheroidal particle and a monochromatic plane-wave incident along the spheroid symmetry axis. The particle and the surrounding medium are taken to be homogeneous, isotropic, and non-magnetic. The theoretical model used is a spheroidal coordinate separation-of-variables solution [15] that allows the computation of the EM fields inside and outside of a spheroid with arbitrary size, shape and complex refractive index. The details of the method are fully described in a previous contribution [3]; therefore, here we only briefly comment on its main features.

By applying the separation of variables to the scalar Helmholtz equation the spheroidal harmonics of EM waves can be obtained [32,33]. The solution of the vector Helmholtz equations for the incident (0), internal (i) and scattered (s) electric $\mathbf{E}$ and magnetic $\mathbf{H}$ fields is determined by expanding the fields in spheroidal vector wave functions obtained from the corresponding scalar spheroidal harmonics. The boundary conditions (BCs) of continuity of the tangential fields across the spheroid surface generate a set of simultaneous linear equations that can be solved for the set of unknown expansion coefficients. The solution of this system of equations is obtained by choosing a suitable truncation number (N) for the fields expansions and then employing the orthogonality integrals approach [15,16,23]. The value of N is chosen to be sufficiently large for convergence of the solution. In each calculation an initial set of expansion coefficients is obtained with the truncation number N = Integer($K_0\alpha$ + 4). Being $K_0 = 2\pi/\lambda$ and $\alpha$ is the longest semi-axis of the spheroid [3,15]. The continuity of the fields' tangential components is then checked at a set of points along the particle surface. If there is not enough rigour in maintaining the BCs in the computed solution, the value of N is progressively increased until an accurate match is obtained between the internal and external tangential fields at the surface.

The total computational time is roughly proportional to $N^3$. Most of this time is spent in the determination of the orthogonality integrals to obtain the expansion coefficients. However, these calculations can be parallelized, scaling down the computational time almost proportionally to the number of CPUs used in parallel. The computational environment used to perform the calculations was Mathematica7.0; suitable due to its high-precision numerical capabilities and its packages for computation of spheroidal harmonics [3,15,33].

Figure 1 is a schematic drawing of the coordinate system used. At axial incidence the illuminating wave ($\mathbf{K_0}$,$\mathbf{E_0}$) can be resolved by a single polarization component, by virtue of symmetry. This wave propagates along the negative $z$ direction with the electric field $\mathbf{E_0}$ parallel to $y$.

In this paper the electric field magnitude is given in units of the incident field amplitude ($E_0$). The length unit used is $\lambda$, making the results given here independent of the particular wavelength of illumination.

The physical parameters involved are the size of the spheroid, its aspect ratio ($b/a$), and the relative refractive index given by the ratio between the refractive index of the particle and that of the ambient medium ($N_r = N_p/N_m$). The spheroid size parameter ($C$) used in the separation-of-variables method is defined in terms of its inter-focal distance $d$ [15,32]:

$$C = \frac{Kd}{2} \tag{1}$$

where $K$ is the wavevector magnitude in the corresponding medium. Inside the particle the size parameter is $C_i = N_rC_0$, being $C_0$ the size parameter in the external medium. Our method allows the computation of the spheroidal harmonics with complex arguments. So, a complex refractive index $N_r = n_r + ik_r$ is considered; enabling us to account for light absorption in the

media [4]. The spheroid size parameter defined in Eq. (1) is not a measure of the spheroid size alone, but rather of the size times the eccentricity of the particle. Therefore, for non-spherical scatterers it is usual to adopt the volume-equivalent-sphere radius ($R_{eq}$) as the characteristic particle size [3,24,31].
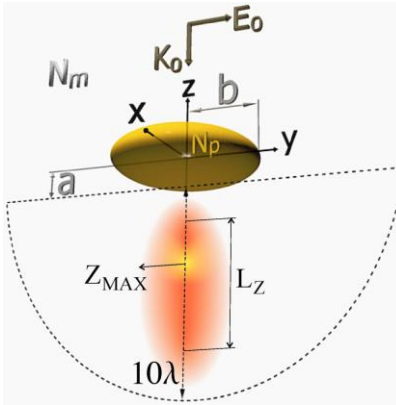


Fig. 1. Coordinate system with origin at the center of the spheroidal particle. The spheroid has semi-axes $a$ ($z$ axis) and $b$ ($xy$ plane). Its refractive index ($N_p$) is higher than that of the surrounding medium ($N_m$). The direction of illumination ($\mathbf{K_0}$) is collinear with the spheroid axis of symmetry ($z$). The scattered light can form a forward-directed lobe extending away from the particle shadow-side surface. The point of highest electric field intensity ($|\mathbf{E}|^2_{MAX}$) outside the particle is located on the $z$ axis at a distance $Z_{MAX}$ from the origin. $L_Z$ is the length of the focal peak along the $z$ axis, corresponding to the distance where the external field intensity remains above $|\mathbf{E}|^2_{MAX}/e^2$.

## 2.1 Numerical limits and computational verification

The main computational challenge of the separation-of-variables approach is the accurate calculation of the spheroidal harmonics for large and complex $C$ values. The method used here [3,15,33] is able to accurately determine the angular harmonics for any $C$, and for high number of orders N. However, the computation of the radial harmonics is limited by numerical cancelation and slow convergence. At present, there appears to be no method that is completely satisfactory for the calculation of these functions for large and complex $C$ [34]. In this work the well-known Wronskian relation was used to check the correctness of the computed radial functions [35]. It was verified that the Wronskian relation is satisfied for absolute values of $C$ below 60. For $|C|>60$ the results may not be accurate enough in some cases. Therefore, the present study is restricted to particles with $|C_i|<60$ in order to avoid possible computational errors associated with the radial functions.

The code used in this paper was extensively checked with known analytic and numerical solutions available in the literature. In a previous contribution [3] the results obtained by our code are shown to match:

• The electrostatic approximation (EA) for a particle size much smaller than λ

• Mie theory for a wavelength-sized sphere

• Far-field scattering patterns of wavelength-sized spheroids presented in [23].

Here, further comparisons with Mie theory are given in Fig. 2.

## 3. Portrait of physical parameters

The field distribution produced by a mesoscopic scatterer is dictated by interference phenomena, and can be conceptually understood by picturing the object as an array of dispersion points, for instance the atoms in a solid [22]. As the incident light beam propagates through the particle material, planes of points transverse to the beam are progressively

illuminated in phase and scattered spherical waves radiate from every point. For each point in a plane radiating spherical waves there is another point in the same plane, separated by a distance of $\lambda/2$, that scatters in opposite phase; and the waves radiated from these two centers cancel in the transverse direction. Thus, in a particle with dimensions comparable or larger than $\lambda$ almost no light is scattered laterally. However, these waves interfere constructively along the direction of propagation and add up to a larger wave inside the particle which propagates along the direction of the illuminating beam, and overlaps with it. When the total internal wave reaches the bottom surface of the particle part of its energy is transmitted to the external medium, and the other part is reflected back to the particle material interfering with itself and undergoing further reflections and refractions at the particle walls.
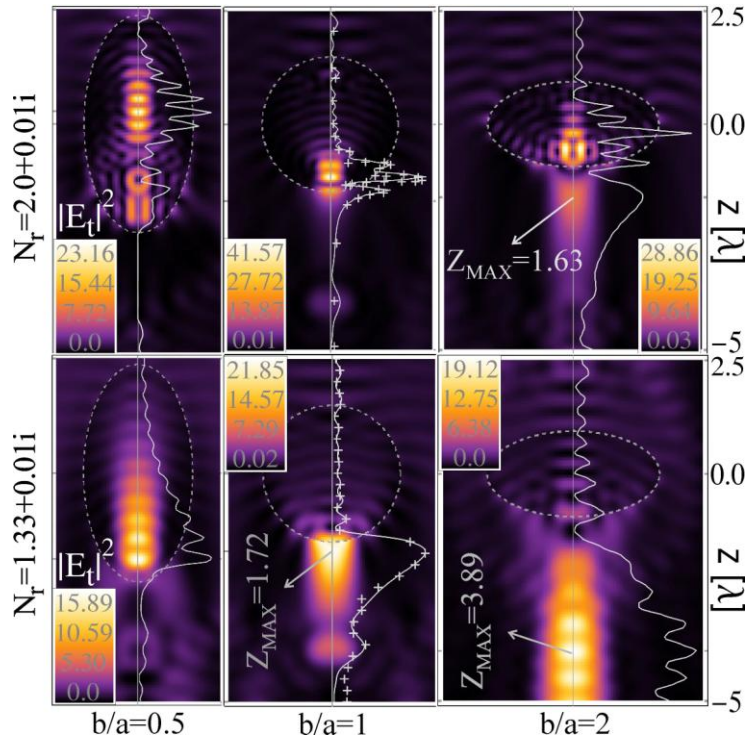


Fig. 2. Total electric field intensity $|\mathbf{E}_t|^2$ distribution, in units of the incident field intensity $|\mathbf{E}_0|^2$, produced by DMPs (outlined with a gray dashed line) with the same size ($R_{eq} = 1.5\lambda$) but distinct aspect ratio ($b/a$) and real part of the relative index ($n_r$). The length unit is $\lambda$. The field distributions were computed on a vertical cross-section through the center of the particle, coplanar with the $yz$ plane defined by the incident wave ($\mathbf{K}_0, \mathbf{E}_0$). The solid curve on the right of each image corresponds to $|\mathbf{E}_t|^2$ along the vertical $z$ axis. The fields in the central plots for spheres ($b/a = 1$) were computed with Mie theory. For comparison, the cross dots in these plots correspond to the values obtained with the spheroidal separation-of-variables method considering spheroids with $b/a = 1.0001$.

The transmitted waves in the external medium propagate along the forward direction and interfere with the waves scattered from the borders of the particle. If the particle has a circular cross-section relative to the incoming light (such as the spheroids considered in this work - see Fig. 1) the path-length difference between the transmitted wave and the scattered waves coming from the circular perimeter of the particle can only lead to constructive interference at a region along the symmetry axis ($z$). This can originate jet-like "focal regions" of high electric field magnitude located close to the shadow-side surface of dielectric mesoscopic particles (DMPs) [6,7,10–12,16,18–20].

Figure 2 displays the total electric field ($\mathbf{E}_t$) intensity distribution produced by DMPs with the same size ($R_{eq} = 1.5\lambda$) but distinct shape ($b/a$) and material ($N_r$). The total field inside the

particle is equal to its internal field ($\mathbf{E_t = E_i}$) and outside it is the sum of the scattered and incident fields ($\mathbf{E_t = E_S + E_0}$). A small imaginary part is considered in the relative refractive index ($k_r = 0.01i$) to account for light attenuation losses of realistic dielectric materials.

In the central plots of spheres ($b/a = 1$) it can be seen that there is a good match between our spheroidal code and Mie theory. The bottom plots ($N_r = 1.33 + 0.01i$) with $b/a = 0.5$ and $b/a = 2$ are similar to those in Figs. 13 and 14 of [16], respectively, which consider lossless materials ($k_r = 0$) and slightly different $R_{eq}$.

The field patterns of Fig. 2 present two main types of modes. The dominant mode outside the particle is the previously described transverse ($\mathbf{E} \perp \mathbf{K}$) wave that propagates in the forward $\mathbf{K_0}$ direction towards the far-field. This mode leads to intensity maxima that can be located inside or outside the particle but always on the $z$ axis. The spot of maximum field ($|\mathbf{E_t}|_{MAX}$) outside the particle is called the focal point, located at a distance $Z_{MAX}$ from the particle center (see Fig. 1). An increase in $Z_{MAX}$ leads to a broadening of the focal region, and to a general decrease in the scattered field intensities. This is observed in the central and right plots of Fig. 2. The more the focus is separated from the particle surface the larger is its waist and length along the $z$ axis ($L_Z$) [7,19]. This occurs because the region of peak constructive interference outside the particle becomes less localized, thus resulting in a wider but less intense focus.

Besides the dominant transverse modes, longitudinal ($\mathbf{E}//\mathbf{K}$) modes are also observed close to the particle surface – the whispering gallery modes [8,19,21]. These modes originate from the total internal reflection of the light inside the particle, making it circulating around its curved surface and interfering with itself. This interference causes discrete peaks around the edge of the particle. The leakage of these peaks outside the particle walls originates longitudinal field maxima in the external medium which evanesce very rapidly ($1/r^3$) with distance ($r$) from the surface. The solutions obtained from Helmholtz equation do not allow the existence of these longitudinal fields on the vertical $z$ axis, but that is not the case in other directions.

### 3.1 Lens-like focusing

Interference effects can lead to regions with significant light concentration in front of the particle; as in the sphere ($b/a = 1$) and oblate ($b/a = 2$) cases of Fig. 2. A smaller volume of constructive interference implies a brighter focus since there is a higher density of electric energy. This resembles the focusing effect of a macroscopic biconvex lens. However, the characteristics (i.e. intensity, position, spatial extension) of such focal spots are distinct from those predicted by geometrical optics (GO) [11,12,21]. The conventional GO focusing by a lens gives focal spots whose dimensions cannot be confined below the wavelength. With DMPs there is not an explicit focus; instead there is a jet-like tail of the scattered intensity along the forward direction which can have sub-wavelength dimensions [7,10,13,18,19]. In GO, the focal distance $f$ of a biconvex lens much larger than $\lambda$ is obtained with the lensmaker equation [14]:

$$f = \frac{n_r R_c^2}{2(n_r - 1)} \cdot \frac{1}{a + n_r(R_c - a)} \tag{2}$$

where $R_c$ is the lens curvature radius, which is equal to $b^2/a$ at the points on the symmetry axis ($z = \pm a$) of a spheroid. It was verified by [10,21] that the values obtained with Eq. (2) only match Mie theory for spheres with radius $R > 20\lambda$, and the lower is $R$ the higher is the discrepancy. Hence, Eq. (2) is not applicable in the mesoscopic size regime; but it can be useful in a qualitative way to elucidate the dependence of the focal distance with the particle parameters. It is straightforward to deduce from Eq. (2) that $f$ decreases with $n_r$ and increases with the spheroid aspect ratio ($b/a$). The same tendencies are observed (see Fig. 2) relative to $Z_{MAX}$ with mesoscopic spheroids [16]. However, the values of $Z_{MAX}$ in the mesoscopic regime are lower than those of $f$ resulting from Eq. (2). The GO lens equation therefore constitutes an upper limit which can be useful for a first-order prediction of a DMP focal distance [11,12].

*3.2 Application in photovoltaics*

The focusing characteristics of the near-field produced by DMPs can be of interest for light management in a growing list of applications, as referred in Section 1. The authors are particularly interested in the implementation of arrays of optimally designed DMPs in photovoltaic (PV) devices [8,36]. The aim is to use such scatterers as "mesoscopic lenses" to improve absorption in the photo-active layers of solar cells. This would enable a reduction in the amount of expensive PV material, an improvement in the conditions for charge carrier collection and a raise in the efficiency by virtue of the concentrated energy density in the PV medium [37]. This is particularly suited for light trapping and concentration in novel solar cell concepts using quantum dots (e.g. intermediate band solar cells [31,38], hot carrier cells, all silicon tandem cells, etc.). DMPs should allow a significant enhancement in the absorption of a single layer of dots within a broad sunlight wavelength range.

Depending on the particular cell architecture, different strategies can be used to position the DMP array in order to take most profit from its forward scattered light. The easiest and cheapest design for practical implementation is to place the particles on the top surface of the cell [8,37]. However, a higher interaction (photocurrent generation) between the PV medium and the scatterers' near-field can be achieved by placing the particles inside the cell material [31,39], for instance in the depletion region of the cell *p-n* junction. It is also possible to have several layers of DMP arrays positioned over distinct layers of a PV device, each array composed of particles designed to concentrate light the way that best suits each layer.

It is important to target the light focusing properties of these structures to the lower energy part of the solar spectrum, the infrared (IR); since the lower energy photons are harder to absorb by typical PV semiconductor materials. The higher energy photons of the visible (VIS) and ultraviolet (UV) range are easily absorbed in the first micrometers of the solar cell material, since their energy is sufficiently higher than the semiconductor bandgap. For these reasons, the complex refractive indices $N_r$ considered in this paper have values that can be physically attainable by common dielectric/semiconductor materials in the IR range. In the optimization studies (Section 4) the domain of the real part $n_r$ was restricted between 1 and 4; and the imaginary part was taken to be $k_r = 0.01$. Nevertheless, the main results are also given for a smaller $k_r = 0.001$ to analyse the effect of lower light attenuation.

When accounting for absorption from the near-field, particular attention has to be paid to the polarization of the scattered light. If the scattered electric field $\mathbf{E_S}$ is longitudinal, energy absorption from this field cannot be determined classically such as with far-fields which are transverse [38]. A longitudinal field is a localized Coulomb field, with no associated Poynting vector [2], that transmits electrostatic energy by means of scalar photons, as described by quantum electrodynamics [40]. This is especially important for particles with sizes much smaller than λ (electrostatic regime) whose peak $E_S$ is longitudinally polarized [31]. However, as the particle size increases and becomes comparable or larger than λ, the transverse component of the region of highest $E_S$ becomes progressively more dominant relative to the longitudinal [3]. So, in the mesoscopic regime the scattered light outside the particle is mostly transverse, having the same polarization as the incident wave [13]. Hence, the classical formalism for light absorption in the far-field can be used here for the absorption produced in the medium located in the DMP near-field. The absorption enhancement due to scattering is therefore given by the ratio between the intensities of the total and incident field ($|\mathbf{E_t}|^2/|\mathbf{E_0}|^2$). This is the quantity represented in the field distributions displayed in this paper.

PV applications also have to account for the unpolarized nature of the illuminating sunlight. The incident field $\mathbf{E_0}$ can take any orientation orthogonal to the propagation direction $\mathbf{K_0}$. Therefore, it is important to have a scatterer shape that allows a response independent of such orientations. That is the case of the spheroids considered here, whose symmetry axis is $\mathbf{K_0}$.

## 4. Results of optimization studies

A Nelder and Mead optimization algorithm was implemented in the analytical EM code described in Section 2, enabling an iterative search for the spheroid parameters that allow a maximum in a certain function of the scattered field. The details of the algorithm are given in the Appendix. Three parameters are used as variables: the spheroid size ($R_{eq}$), aspect ratio ($b/a$) and real part of the relative refractive index ($n_r$). The imaginary part of the relative index is kept fixed ($k_r = 0.01$). Two particular functions were considered for optimization that maximize at quite distinct near-field patterns; thus providing a good illustration of the different ways in which DMPs can be used for light concentration. The results obtained for each function are given in the following Sections 4.1 and 4.2.

### 4.1 Optimization of local electric field intensity

The first function to be optimized is the maximum of the scattered field intensity ($|\mathbf{E_S}|^2/|\mathbf{E_0}|^2$) at any point in the external medium in front of the particle. Three particular cases are considered:

1) Sphere ($b/a = 1$), using $R$ and $n_r$ as variables

2) Spheroid with $n_r = 1.33$, using $R_{eq}$ and $b/a$ as variables

3) General spheroid using $R_{eq}$, $b/a$ and $n_r$ as variables

The results obtained in each case are presented in the following sub-sections and summarized in Table 1. For the three cases the optimization converged to localized focal regions at the bottom surface of the particle in the $z$ axis ($Z_{MAX} = a$). That is the spot where the focus can be more confined outside the particle; thus allowing the highest possible field magnitude in the external medium.

**Table 1. Characteristics of the Optimal Spheroids
That Maximize the Scattered Field Intensity[a]**

| Optimization of Scattered Intensity | Optimal Parameters | | | $\|\mathbf{E_t}\|^2_{MAX}$ (at $z = -a$) | | $L_Z$ Focal Length[b] |
|---|---|---|---|---|---|---|
| | $n_r$ | $R_{eq}$ | $b/a$ | $k_r = 0.01$ | $k_r = 0.001$ | |
| Sphere | 1.733 | 5.785 | 1.0 | **92.06** | 328.3 | 1.39λ |
| Spheroid with $n_r = 1.33$ | 1.33 | 3.446 | 0.773 | **46.79** | 99.21 | 2.71λ |
| General spheroid | 4.0 | 1.415 | 1.461 | **110.7** | 176.4 | 0.13λ |

[a]The values in green are the parameters that remained fixed. The optimizations were performed with a fixed $k_r = 0.01$; however $|\mathbf{E_t}|^2_{MAX}$ is also given for the case of $k_r = 0.001$ with the same spheroid parameters.
[b]Width of the $|\mathbf{E_t}|^2$ peak along the $z$ axis measured outside the particle (from $z = -a$ to the point where $|\mathbf{E_t}|^2 = |\mathbf{E_t}|^2_{MAX}/e^2$).

### 4.1.1 Sphere case

We start by presenting the results for the maximization of the scattered intensity produced by spherical particles ($b/a = 1$) with variable radius $R$ and $n_r$. Since the geometry is spherical the fields were computed with Mie theory to save computational time.

For a given $R$, the lower is $n_r$ the higher is the distance of the focus to the particle center, as predicted by the lens Eq. (2). The focus can therefore be located inside or outside the particle depending on the value of $n_r$. As observed in [10,21], the maximum field intensity outside the particle always occurs for the $n_r$ index that sets the focal point right at the particle surface ($Z_{MAX} = R$). According to Eq. (2), for macroscopic spheres the value of $n_r$ that sets $f = R$ is $n_r = 2.0$. With mesoscopic spheres such $n_r$ value is too high since it places the maximum intensity inside the particle [10,11], as shown in the central top plot of Fig. 2. A smaller $n_r = 1.33$ (see central bottom plot of Fig. 2) is already too low because it sets the maximum $E_t$ outside the particle separated from its surface. The optimal values of $n_r$ that place the focus exactly at $z = -R$ are plotted in Fig. 3(a) (dashed line) for $R$ ranging from 0.5λ to 10λ. The optimal $n_r$ is around $\sqrt{3}$ within such mesoscopic sizes, and tends to 2.0 as the size approaches the macroscopic GO regime [10,11].

The field intensities at the focal point ($|\mathbf{E_t}|^2_{MAX}$) are shown in Fig. 3(a) for $k_r = 0.01$ and $k_r = 0.001$ (solid lines) using the optimal $n_r$. The attenuation index $k_r$ has a quite significant impact in the peak field magnitudes that can be obtained in these optimal cases. If absorption were neglected ($k_r = 0$), the bigger the sphere size the stronger could be the focal point intensity. The effect of absorption opposes this tendency, because the bigger the particle the more energy is dissipated in its volume and thus the less energy is available for the focus. As shown in the solid curves of Fig. 3(a), for low sizes $|\mathbf{E_t}|^2_{MAX}$ increases with $R$. However, for sufficiently big $R$, the effect of absorption dominates over scattering and $|\mathbf{E_t}|^2_{MAX}$ starts decreasing with the size. The higher is $k_r$ the lower is the optimal $R$ value at which the maximum in the curves occurs. For $k_r = 0.01$ such maximum is at $R_{opt} = 5.785\lambda$, which matches the result obtained with the optimization algorithm. The electric field intensity distribution of this case is plotted in Fig. 3(b). At the particle surface ($z = -R$) the intensity is $|\mathbf{E_t}|^2_{MAX} = 92.06$, but with lower $k_r = 0.001$ it is about 3.5 times higher ($|\mathbf{E_t}|^2_{MAX} = 328.3$).
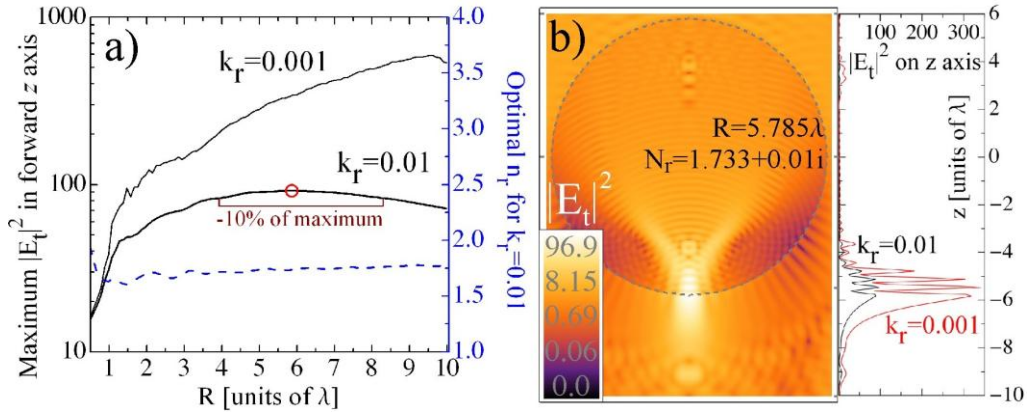


Fig. 3. **(a)** *Left axis (black curves)* - Maximum values of $|\mathbf{E_t}|^2$ (in units of $|\mathbf{E_0}|^2$) outside the particle, as a function of the sphere radius ($R$), for $k_r = 0.01$ and $k_r = 0.001$. The red circle is at the value obtained with the optimization algorithm considering $k_r = 0.01$. The line segment beneath the circle marks the interval where $|\mathbf{E_t}|^2$ remains within a 10% difference from the maximum value. *Right axis (blue curve)* - Optimal $n_r$ values computed with $k_r = 0.01$. Similar values are obtained with $k_r = 0.001$. **(b)** *Left* - $|\mathbf{E_t}|^2$ distribution, in logarithmic scale, for the optimal sphere parameters ($R,n_r$) indicated in the plot. The distribution is computed on the same $yz$ plane as those of Fig. 2. *Right* - $|\mathbf{E_t}|^2$ along the $z$ axis, in linear scale, for $k_r = 0.01$ (*black line*) and $k_r = 0.001$ (*red*).

A DMP fabricated with the optimal parameters of Fig. 3(b) would produce a focal intensity above $0.9|\mathbf{E_t}|^2_{MAX}$ for any wavelength within $\lambda \pm 0.3\lambda$. This broad frequency width is due to the fact that the $k_r = 0.01$ curve in Fig. 3(a) is rather flat around $R_{opt}$ (as marked by the line segment beneath the curve), and $n_r$ remains approximately constant in that interval.

4.1.2 Spheroid with $n_r = 1.33$

A relative refractive index of 1.33 is often adopted in theoretical studies of particle scattering [4,7,15,16,23,24,28]. This is the refractive index of water in air, but can also match other possible particle/medium material combinations. For instance, a germanium particle in a gallium arsenide or silicon medium corresponds to a relative index close to that value in the infrared, which can be interesting for PV applications. In this case there is a small imaginary part in the refractive index on the order of $k_r = 0.01i$, as considered in this work.

In this sub-section we present the optimization of the scattered intensity produced by spheroidal particles with a fixed refractive index ($N_r = 1.33 + 0.01i$) but tunable size ($R_{eq}$) and aspect ratio ($b/a$). The optimal geometry is plotted in Fig. 4. The maximum field intensity ($|\mathbf{E_t}|^2_{MAX} = 46.8$) occurs at the bottom point of the particle ($z = -a$), such as in the previous sphere case. With lower attenuation ($k_r = 0.001$) the maximum field at that spot increases to about twice this value ($|\mathbf{E_t}|^2 = 99.2$), as shown in the right plot of Fig. 4.

The optimization converged to a prolate geometry since only with $b/a<1$ could the focus be positioned at the particle surface given such low $n_r$. If the shape were spherical or oblate the focal region would be located away from the surface (see bottom plots of Fig. 2) exhibiting higher length but lower peak intensity. For comparison, the maximum intensity produced by a sphere with the same $R_{eq}$ and $N_r$ as the prolate of Fig. 4 is $|\mathbf{E}_t|^2 = 33.9$ at $Z_{MAX} = 4.29\lambda$.
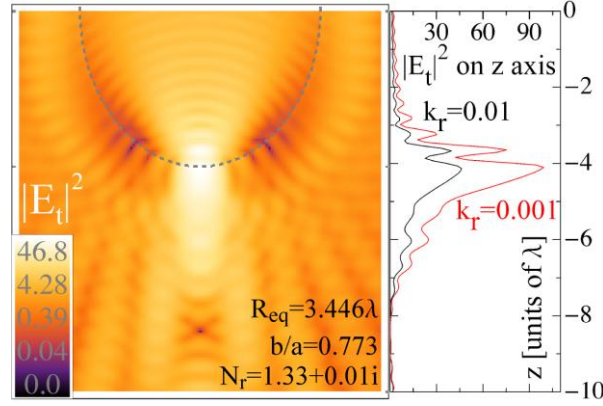


Fig. 4. Same as Fig. 3(b) but for the optimal spheroid geometry with a fixed $n_r = 1.33$ and variable $R_{eq}$ and $b/a$. The dimensions of the spheroid semi-axes are: $a = 4.093\lambda$ and $b = 3.162\lambda$.

### 4.1.3 General spheroidal case

The optimization is now extended to the general case of a spheroidal particle with variable size ($R_{eq}$), aspect ratio ($b/a$) and real part of the relative index ($n_r$). The domain of variation of $n_r$ was restricted to $n_r \leq 4.0$, since most pure or compound dielectric materials have refractive indices lower than such limit at low optical frequencies, as referred in Section 3.2. The imaginary part of $N_r$ is kept fixed ($k_r = 0.01$).

As in the previous cases, the optimization converges to spheroid parameters that locate the focal spot at the particle bottom surface ($z = -a$). In addition, the search moves towards the highest allowed $n_r$ value ($n_r = 4.0$). A higher $n_r$ increases the optical interference inside the spheroid, since the internal light waves have smaller wavelength and suffer more refraction and reflection with the particle walls. The combination of these effects raises the intensities associated with the concentrated field at the spots of constructive interference [27,30].

Increasing $n_r$ also shifts the maximum field intensity towards the particle interior. Therefore, usually DMPs with big $n_r$ exhibit high internal fields but small scattered intensities in the external medium. This is, for instance, the case of spheres with any $n_r$ above the optimal values given in Fig. 3(a). Nevertheless, with spheroids there is an additional degree of freedom, the aspect ratio, which enables to keep the focus outside the particle while still using a high refractive index. This constitutes one of the main advantages of spheroids for near-field light concentration, and a key point of this paper. As displayed in Fig. 2, the effect of the aspect ratio on the location of the focal spot is opposite to the effect of $n_r$. Thus, the focus can be kept at the bottom point of the particle ($Z_{MAX} = a$) if $b/a$ is increased together with $n_r$. This possibility allows the achievement of near-field intensities of more than two orders of magnitude (relative to the incident intensity) and with spheroid sizes lower than those of Sections 4.1.1 and 4.1.2.

In the present case, the optimization converged to an oblate ($b/a>1$) shape, since otherwise the maximum $|\mathbf{E_t}|^2$ would be inside the particle for such high $n_r = 4.0$. The corresponding field pattern is given in Fig. 5. As shown in the right plot, the curve corresponding to $k_r = 0.001$ has a maximum $|\mathbf{E_t}|^2 = 176.4$, which is 1.6 times higher than the peak value of $k_r = 0.01$. The ratio between the values of $|\mathbf{E_t}|^2_{MAX}$ for $k_r = 0.001$ and $k_r = 0.01$ is lower in this case than in the previous cases of Figs. 3(b) and 4 (see Table 1). This is due to the fact that a smaller spheroid

size reduces the effect of light absorption by the particle material. For the same reason, the ratio between the $|\mathbf{E_t}|^2_{MAX}$ in Fig. 4 is smaller than that in Fig. 3(b).

The pronounced interference caused by this high $n_r = 4.0$ results in a more confined focal spot than that of the field distributions in Figs. 3(b) and 4 (see $L_Z$ values in Table 1). The focal peak is extremely localized in this case, having sub-wavelength dimensions both in the $z$ ($L_Z = 0.13\lambda$) and $y$ ($L_Y = 0.54\lambda$ - see inset in Fig. 5) directions. Spherical DMPs can also produce external focal regions that are sub-wavelength confined in the transverse $xy$ directions, but not along the forward $z$ axis when illuminated by a plane-wave [10,11,17,19,20]. With oblate DMPs having a high $n_r$ it is possible to achieve sub-wavelength confinement with plane-wave illumination both in the transverse and forward directions.
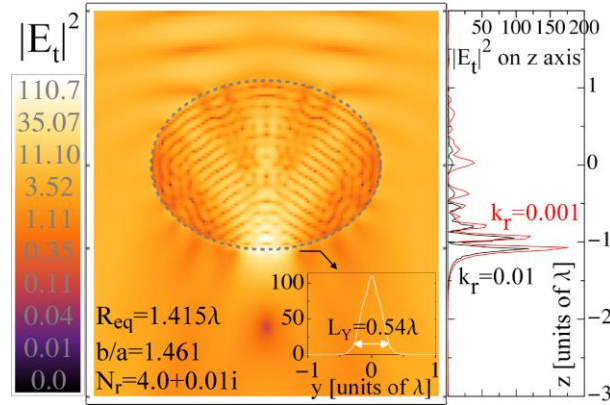


Fig. 5. Same as Fig. 3(b) but for the optimal spheroid parameters obtained with tunable $R_{eq}$, $b/a$ and $n_r$. The dimensions of the spheroid semi-axes are: $a = 1.099\lambda$ and $b = 1.605\lambda$. The bottom inset shows the peak $|\mathbf{E_t}|^2$ along $y$ at the bottom of the particle ($z = -a$). $L_Y$ is the peak full width at $|\mathbf{E_t}|^2 = |\mathbf{E_t}|^2_{MAX}/e^2$.

### 4.2 Optimization of electric intensity over near-field region

A second class of optimizations was performed to find the spheroid parameters that maximize the integral of the scattered intensity over the near-field region in front of the particle. The aim here is not to achieve a high field magnitude at a certain point, like in the previous cases, but rather to find the highest possible scattered field distribution with a broad focal region in front of the particle. This can be of interest for applications, such as PV, that can benefit from a wide region of light concentration extending throughout the volume of a nearby absorbing medium. The near-field zone around a scatterer with size close to $\lambda$ extends up to a distance on the order of $10\lambda$. Therefore, the function to be optimized (P) integrates the scattered intensity, normalized by $|\mathbf{E_0}|^2$, along a semi-circular region in front of the particle, in the $yz$ plane, of radius $R_M = 10\lambda$:

$$P(R_{eq}, b/a, n_r) = \frac{1}{\pi ab} \iint \frac{|E_s|^2}{|E_0|^2} f(\eta, \xi) d\eta d\xi \qquad (3)$$

Here $\eta$ and $\xi$ are the spheroidal angular and radial coordinates, respectively; and the factor $f(\eta, \xi) d\eta d\xi$ is the area element in spheroidal coordinates. The region of integration is outlined by the dashed semi-circle in Fig. 1. The radius of this region ($R_M$) is on the order of the thickness of the main photocurrent generation zone in most solar cell designs, considering $\lambda \approx 1\mu m$ (near-IR). As such, function P is an example of an optimization function suited to find the best spheroid parameters for implementation in PV devices. DMPs can be incorporated either on top of solar cells or embedded in their PV material, depending on the cell architecture and the preferred relative refractive index. In any case, the particles size should be as small as possible since their material always constitutes a disturbance in the PV medium

which only serves for optical concentration purposes but cannot contribute (and most of the times deteriorates) to the current generation. If DMPs designed to focus IR light are placed on top of a cell the bigger their size the more significant becomes their attenuation of the lower wavelengths (VIS and UV), reducing the cell response to the higher energy part of the solar spectrum. This issue can be avoided if DMPs are placed inside the PV material. Nevertheless, in such case the bigger the DMP size the more volume of PV medium is occupied and the higher is the charge carrier trapping that may occur at the particle-medium interface.

In view of the above, the area integral in Eq. (3) is normalized by the $yz$ area of the particle ($\pi ab$), in order to beneficiate smaller sizes ($R_{eq}$) in the optimization procedure.

In the following sub-sections we present the results obtained with the optimization of Eq. (3) considering the same 3 cases (sphere, spheroid with $n_r = 1.33$ and general spheroid) of Section 4.1. The main results are summarized in Table 2.

**Table 2. Characteristics of the Optimal Spheroidal Parameters That Maximize Function P$^a$**

| Optimization of Function P | Optimal Parameters | | | $P_{MAX}$ | $(\pi ab)P_{MAX}$ | $L_Z$ Focal Length$^b$ |
|---|---|---|---|---|---|---|
| | $n_r$ | $R_{eq}$ | $b/a$ | | | |
| Sphere | 1.287 | 1.195 | 1.0 | **15.35** | 68.86 | 2.19$\lambda$ |
| Spheroid with $n_r = 1.33$ | 1.33 | 1.642 | 3.380 | **36.28** | 204.7 | 7.71$\lambda$ |
| General spheroid | 4.0 | 0.741 | 28.75 | **278.8** | 157.1 | 8.04$\lambda$ |

$^a$The values in green correspond to the parameters that remained fixed. The optimizations were performed with a fixed $k_r = 0.01$.
$^b$Focal peak width along the $z$ axis (see Fig. 1).

### 4.2.1 Sphere case

As in Section 4.1.1, the calculations for spherical particles were performed with Mie theory for faster computation. In this case the aspect ratio is fixed ($b/a = 1$), so the quantity P (Eq. (3)) becomes a function of only two parameters: $R$ and $n_r$. As before, the imaginary part of the refractive index is kept fixed ($k_r = 0.01$).
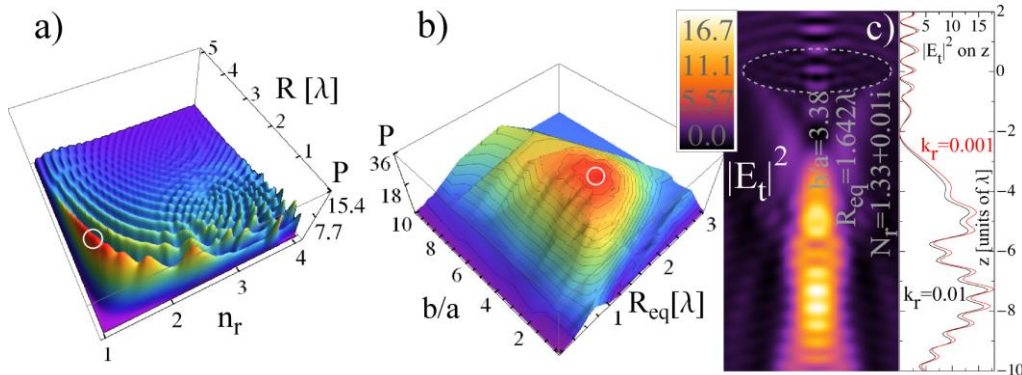


Fig. 6. **(a)** 3D plot of the optimization function P($R,n_r$) for spheres. The white circle is at the spot of maximum P obtained with the optimization algorithm. **(b)** Same as (a) but for the optimization of spheroids with fixed $n_r = 1.33$ and tunable $R_{eq}$ and $b/a$. **(c)** $|E_t|^2$ distribution, in linear scale, corresponding to the optimum spheroid parameters indicated by the white circle in (b). The spheroid semi-axes are: $a = 0.729\lambda$ and $b = 2.464\lambda$.

The two parameters can be viewed as the coordinates of a bi-dimensional space in which P($R,n_r$) is to be maximized. Figure 6(a) shows the values of P for every ($R,n_r$) point within the search domain of the optimization algorithm. There are several local maxima in the function whose intensity becomes progressively lower with increasing $R$ and $n_r$. The decrease of P with $R$ is mainly due to the normalization factor $(\pi ab)^{-1}$ multiplying the integral in Eq. (3). As previously referred, our aim here is to find the scatterer parameters that achieve the highest possible electric field integral with a particle that occupies the least possible volume; as an exercise for possible PV applications. Nevertheless, the values of the integral alone ($\pi ab P_{MAX}$)

are also given in Table 2 for the optimal parameters. The P peaks decrease with $n_r$ because the focal region moves towards the particle interior, thus reducing the scattered intensity in the external medium in front.

The global P maximum obtained with the optimization is marked by a white circle in Fig. 6(a). This peak is rather flat along the $R$ axis close to the optimal value $R_{opt} = 1.2\lambda$, as in the curve of $k_r = 0.01$ in Fig. 3(a). Therefore, a sphere fabricated with the optimal parameters produces a P value above $0.9P_{MAX}$ at any wavelength within $\lambda \pm 0.2\lambda$.

### 4.2.2 Spheroid with $n_r = 1.33$

The present case with a low relative refractive index $N_r = 1.33 + 0.01i$ can be interesting for applications that benefit from a small material contrast between scatterer and surrounding medium. That is the case of PV applications in which the particles are embedded inside the PV medium. In that situation the lower is $N_r$ the less charge carrier trapping and recombination occurs at the particle surface.

Figure 6(b) represents function $P(R_{eq}, b/a)$ in a region around its maximum value obtained with the optimization. Function P decreases with $R_{eq}$ due to the normalization of the integral in Eq. (3) by the spheroid area. The aspect ratio ($b/a$) shifts the position and spatial extension of the focal region. High aspect ratios not only reduce the overall scattered intensities but can also place the jet-like focus too far in $z$, outside the integration region limited by the dashed line in Fig. 1. If $b/a$ is too small the focus moves close to the particle and becomes more spatially confined; which may produce higher peak intensities at the focal spot (such as in Fig. 4) but a lower value of the integral of $E_S$ over the chosen semi-circular region.

The maximum P occurs for the field distribution displayed in Fig. 6(c). The $R_{eq}$ width of the peak P in Fig. 6(b), within $-10\%$ of the maximum, allows a wavelength variation of $\lambda \pm 0.21\lambda$; which is close to that reported in the previous sub-section. It can be seen in the right plot of Fig. 6(c) that there is a quite small difference between the $|\mathbf{E_t}|^2$ profile of $k_r = 0.01$ and $k_r = 0.001$, as compared with the previous cases of Section 4.1.

### 4.2.3 General spheroidal case

The optimization of P with all 3 parameters ($R_{eq}, b/a, n_r$) achieves a value ($P_{MAX} = 278.8$) considerably higher than the previous two cases, as indicated in Table 2.
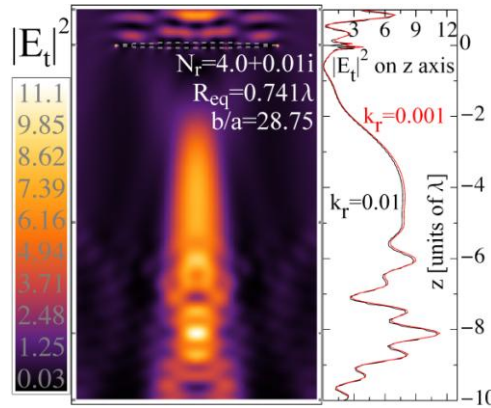


Fig. 7. *Left* - $|\mathbf{E_t}|^2$ distribution for the optimal parameters that maximize function $P(R_{eq}, b/a, n_r)$. The spheroid semi-axes are: a = 0.079λ and b = 2.271λ. *Right* - $|\mathbf{E_t}|^2$ profiles along the $z$ axis for $k_r = 0.01$ (*black line*) and $k_r = 0.001$ (*red*).

As in Section 4.1.3, the algorithm converges to the highest allowed refractive index ($n_r = 4.0$) since the higher is $n_r$ the higher can be the scattered field outside the particle. However, the increase of $n_r$ has to be accompanied by an increase in $b/a$ or else the focal region moves too close to the particle (or even to its interior) and loses its extension over the near-field region in front. Keeping the highest possible $n_r = 4.0$ and large $b/a$, the algorithm converges to

small particle sizes ($R_{eq} < \lambda$) in order to achieve a high value of the integral in Eq. (3) with a low value of the spheroid $yz$ area ($\pi ab$) in the denominator.

The spheroid parameters that allow a maximum in $P(R_{eq}, b/a, n_r)$ produce the field distribution shown in Fig. 7. An oblate with such extreme elongation presents a long forward scattering lobe; quite distinct from the point focus obtained with the moderately elongated oblate in Fig. 5. It can be seen in the right plot of Fig. 7 that there is almost no difference between the field intensities with $k_r = 0.01$ and $k_r = 0.001$, due to the small particle size.

Even higher P values could be achieved with higher values of the size parameter $C_i$. As referred in Section 2.2, the maximum allowed value of $|C_i|$ was limited to 60 in order to avoid inaccuracies in the calculation of the radial spheroidal harmonics.

## 5. Conclusions and final remarks

The relation between the geometry and material of a spheroidal scatterer and its resulting field distribution may be very complex; especially in the mesoscopic regime where it can only be analytically determined by fully solving Maxwell's equations using the continuity BCs across the particle surface. This can be accomplished by the spheroidal coordinate separation-of-variables method used here, described in Section 2 and further detailed in [3,15].

The results of this paper illustrate the capabilities of spheroidal DMPs for use as "mesoscopic lenses" in PV or in several other applications (listed in Section 1). For the first time, an optimization algorithm was coupled to the analytical EM code to iteratively search for the scatterer parameters that allow the maximization of a certain function of the scattered field. Two different quantities were considered for optimization: 1) the value of the scattered intensity at any point outside the particle (Section 4.1); 2) the integral of the scattered intensity over a semi-circular region in front of the particle of radius $10\lambda$ (Section 4.2). These two particular functions chosen here converge to quite distinct near-field distributions.

With the first function, the maximum intensity in the external medium is achieved by placing the focus right at the point of intersection between the particle surface and the $z$ axis. The higher $n_r$ the more intense and confined can the focus be. However, the particle *oblateness* has to increase with $n_r$ or else the light would be focused in the interior of the particle. An optimal adjust of $b/a$ and $n_r$ can lead to electric field intensities at the particle surface of more than 2 orders of magnitude higher than the incident intensity, with a particle size close to $\lambda$ (see Fig. 5). Such pronounced intensities are achieved due to a sub-wavelength confinement of the focal peak in all directions, which is possible in plane-wave illumination with an oblate geometry and high $n_r$. This is one of the main advantages of going beyond the simple spherical geometry with the use of spheroidal DMPs; and can be interesting for applications with localized absorbing centers, such as quantum-dot solar cells [31].

The second function converges to wide focal regions extending several $\lambda$ along the $z$ axis. The electric intensities are not as high as in the previous case, since the energy is distributed in a bigger volume of the external medium. This situation can be advantageous for certain applications, such as most types of thin-film solar cells [36], that benefit from an extended region of field enhancement covering a broad portion of the surrounding absorbing medium.

Pronounced near-field light amplification can also be achieved in the electrostatic regime using the surface plasmon resonance (SPR) of metallic nanoparticles (MNPs) much smaller than $\lambda$ [5,31,36–38]. As shown here, the electric intensity enhancement that can be obtained with mesoscopic spheroids is as high as that predicted at the surface of MNPs sustaining SPRs ($\sim 100 E_0^2$) in the infrared. Nevertheless, DMPs may be more suited for certain applications, such as PV, due to the following additional advantages [3]:

First, since they are composed of dielectric material their inclusion in the interior of the photo-active medium of a solar cell should cause less current degradation (due to charge carrier recombination at the particle surface) than MNPs [8,37]. Secondly, the scattering pattern produced by MNPs has a single dipolar (first-order) mode. DMPs excite additional higher-order modes thereby allowing very distinct near-field profiles which can be adapted to different structures of the device absorber. The intensity, spatial extension and position of the peak field intensity can be adjusted by tuning the particle parameters, as explained in this

paper. Thirdly, besides higher spatial extension, there is also a higher frequency extension of the electric field peaks produced by DMPs. The SPR resonance produces sharp intensity peaks having a HWHM of about $0.1\lambda$. With DMPs the peaks can be broader in wavelength; the examples analysed here have half widths of $0.2\text{-}0.3\lambda$ relative to only $-10\%$ of the maximum.

Nevertheless, there are also a few drawbacks that can limit the application of DMPs in practical devices. One of the disadvantages is that the precise conditions (size, shape and material) that allow DMPs to perform optimally as light concentrators may be hard to fabricate. There are also challenges related with the construction of an array of spheroidal particles on a device material. Due to the aspherical shape of the particles, colloidal deposition techniques such as spin or dip-coating may not be feasible since it is hard to control the orientation of the particles upon deposition. Possible mass production alternatives are litographical techniques for large-scale patterning, such as hollographic litography (HL) or hole-mask colloidal litography (HCL). However, perhaps the main disadvantage is the complexity of the calculations required to model their optical response; requiring considerable computational time and resources. That is the reason why the mesoscopic size regime hasn't been much explored beyond Mie theory studies limited to spherical geometries. This introduces challenges to new optical approximations [11,24,25,41] and motivates the development of more efficient numerical models to improve the speed and accuracy of the computed EM solutions [3,15,26].

## Appendix - Nelder and Mead optimization algorithm

The optimization routine used in this work consists of a multidimensional direct search algorithm known as the Nelder and Mead method [42,43]. The method determines the set of $n$ variables that maximize (or minimize) a certain function $F$. The $n$ variables are treated as the coordinates of a $n$-dimensional space in which $F$ is defined. The algorithm starts by picking $n+1$ initial points inside the $n$-dimensional domain. These points are regarded as the vertices of an $n$-simplex ($n$-dimensional analogue of a triangle). Function $F$ is evaluated at each of these vertices and then the algorithm moves and/or redimensions the $n$-simplex in the $n$-dimensional space towards the vertex with better $F$ value. Function $F$ is again evaluated at the new $n$-simplex points and the procedure is iteratively repeated as better $F$ values are found, until some desired bound is obtained.

It is important to define well the domain (lower and upper limits) of each $n$ variable, in order to avoid searching in physically forbidden regions, or where it is known that $F$ has undesired values. The optimizations performed in this work use up to 3 variables, the spheroid parameters: $R_{eq}$, $b/a$ and $n_r$. The domain allowed for the simplex was defined according to a set of lower limits ($a,b>0$ and $n_r>1$) and upper limits ($n_r\leq4.0$ and $|C_i|<60$). The upper limit for $n_r$ was taken to be 4.0 for the reasons mentioned in Section 3.2. The upper bound set for $|C_i|$ is due to computational constraints, as referred in Section 2.2.

The points chosen for the initial simplex were picked randomly inside the allowed domain. The algorithm then moves and redimensions the simplex towards the regions of highest $F$ until it shrinks at the maximum point found. With this method a maximum is reached within about 30-50 iterations. However, this can be a local maximum in the search domain. To ensure that a global maximum is reached, the algorithm is sequentially run with different initial point sets until the results converge to a single overall maximum. Tables 1 and 2 present the values of the overall maximum values obtained for the optimizations of $|\mathbf{E_S}|^2$ and P (Eq. (3)), respectively.

## Acknowledgments